Journal of Structural Geology 39 (2012) 199–209

Contents lists available at SciVerse ScienceDirect

Journal of Structural Geology

journal homepage: www.elsevier.com/locate/jsg

Localization patterns in sandbox-scale numerical experiments above a normal fault in basement

Sofie Nollet [a,c,*], Gisa J. Kleine Vennekate [b], Steffen Giese [b], Peter Vrolijk [c], Janos L. Urai [a], Martin Ziegler [b]

[a] RWTH Aachen, Structural Geology, Tectonics and Geomechanics, Lochnerstr. 4-20, 52056 Aachen, Germany
[b] RWTH Aachen, Chair of Geotechnical Engineering, Mies-van-der-Rohe-Str. 1, 52074 Aachen, Germany
[c] ExxonMobil Upstream Research Company, P.O. Box 2189, Houston, TX 77252-218, USA

ARTICLE INFO

Article history:
Received 23 June 2011
Received in revised form
7 February 2012
Accepted 22 February 2012
Available online 3 March 2012

Keywords:
Numerical modeling
Finite element
Localization
Faulting
Sandbox

ABSTRACT

The finite element program ELFEN is used to study the effect of basement fault dip on the evolution of shear band patterns in unconsolidated sand. The material properties and boundary conditions of the model were chosen to correspond to generic sandbox experiments.

Model results reproduce the range of structural styles found in corresponding sandbox experiments. With a basement fault dip of 60° and lower, a graben structure is formed, composed of a synthetic shear band followed by one or more antithetic shear bands. With a basement fault dip of 70° and steeper, a reverse (precursor) shear band forms first, followed by a synthetic, normal shear band that accommodates all further displacement. The dip of the synthetic shear band is close to the basement fault dip. For basement fault dips between 60° and 70°, we observe a transition in localization patterns. An analysis of the stress fields and velocity vectors in the model explains the first-order aspects of the relationships observed.

We consider the observed 'precursor-dominated' and 'graben-dominated' *structural domains* to be important components of normal fault systems in which the first order structural style and deformation patterns are only weakly dependent on the details of the rheology of the model materials and explore the interesting problem of the change in structural style from 'precursor-dominated' to 'graben-dominated' *structural domains* above a normal fault in basement. We find similar *structural domains* in sandbox experiments for the same set of boundary conditions but with slightly different material properties, suggesting that the modeled patterns are robust within these two *structural domains*, (i.e. will occur over a range of similar material properties and boundary conditions).

The results of this study contribute to our ability to validate numerical models against experiments in order to finally better simulate natural systems.

1. Introduction

In many sedimentary basins, sediments cover a faulted basement. In contrast to co-seismic faults, where stress changes cyclically (e.g. Nuechter and Ellis, 2010), the faults resulting in these sediments are more slowly moving and stress conditions approximate steady-state conditions. The location and the geometry of deformation in the overlying sediments is strongly dependent on these major basement faults and lineaments (e.g. Richard, 1991; Higgins and Harris, 1997; Bailey et al., 2005; Hardy, 2011; Taniyama, 2011). More specifically, sandbox experiments that model deformation in sand above a basement fault have demonstrated that the basement fault dip has an important impact on the resulting shear band pattern (Sanford, 1959; Horsfield, 1977; Tsuneishi, 1978; Withjack et al., 1990; Patton, 2005; Schöpfer et al., 2007a, b). Two classes of structural evolution have been observed in these studies, with "precursor-dominated" and "graben-dominated" shear band patterns. It is unclear which parameters control the change between these patterns and whether the experiments can be scaled to predict fault structures in nature (Mandl, 2000).

A method to explore this parameter space efficiently is through the use of numerical simulations (Kenis et al., 2005; Abe et al., 2011; Abe and Urai, 2012). However, it is an unsolved challenge to assign the appropriate constitutive relations with a complete set of accurately and independently measured material parameters in an attempt to achieve an exact correspondence between sandbox and numerical experiments.

* Corresponding author. RWTH Aachen, Reservoir-Petrology, Wüllnerstraße 2, 52056 Aachen, Germany. Tel.: +49 241 80 98273.
E-mail addresses: sofie.nollet@emr.rwth-aachen.de, sofie.nollet@gmail.com (S. Nollet).

0191-8141/$ – see front matter © 2012 Elsevier Ltd. All rights reserved.
doi:10.1016/j.jsg.2012.02.011

Here, we present a series of numerical models of the effect of basement fault dip on the evolution of shear bands in sandbox experiments. In this study we make the implicit assumption which is made in all similar modeling studies (e.g. modeling results in the BENCHMARK project, Buiter et al., 2006) that the first-order structural style and shear band patterns are only weakly dependent on the details of the rheology of the model materials within the corresponding fields of material properties. Therefore, within these fields, both sandbox experiments and numerical models tend to produce similar, i.e. robust patterns of shear bands that compare to faults in natural prototypes.

We define a *structural domain* as a set of faults or shear bands that develop with similar geometric and temporal characteristics. In our study of the effects of changing fault dip, we relate shear band geometry to the orientation of basement fault, to identify different *structural domains*, and we infer that corresponding *domains* are present in other deformation systems.

Geomechanical models also complement sandbox models by serving as the foundation upon which a deeper physical understanding of fault processes is built. For example, in previous work by Adam et al. (2005) , Holland et al. (2006), van der Zee et al. (2008), Schmatz et al. (2010), van Gent et al. (2010a,b) and Holland et al. (2011), it was shown that experiments which included the formation of precursors in layered models produced significant complexity in the evolving fault zone, such as relays, lenses and lateral variations in thickness of clay smear.

To the extent that the evolution of localization patterns dictates fault zone internal structure, it becomes imperative to understand the primary controls on different *structural domains*.

2. Methods

Traditional continuum modeling methods have limited capabilities for modeling spontaneous localization and large displacements on faults because of distortion of the numerical grid (e.g. Schultz-Ela and Walsh, 2002; van der Zee et al., 2003). Recent advances in numerical methods (both finite element and discrete particle modeling) now allow strains and displacements similar to those produced in sandbox experiments (e.g. Ellis et al., 2004; Panien et al., 2006; Crook et al., 2006, Gudehus and Karcher, 2006; Schöpfer et al., 2007a, b, Schöpfer et al., 2009a, b; Welch et al., 2009).

The finite element modeling approach in ELFEN is based on a quasi-static, explicit Lagrangian method with automated remeshing (Crook et al., 2006). The constitutive law for sand provides a hardening/softening model for the evolution toward a critical state surface where constant-volume plastic flow occurs at constant effective stress. This constitutive law is able to reproduce the experimentally observed response of sands in confined triaxial tests at large strains for a wide range of initial stress conditions, in contrast to the more commonly used Mohr-Coulomb constitutive models (e.g. van der Zee and Urai, 2005). This allows localization of deformation in the continuum, however the energy dissipation in the deformation bands is sensitive to the scale of the discretization. In other words, solutions depend on the element length scale rather than a physical material length scale. To avoid this, a fracture energy approach is included in the constitutive law that limits the global energy dissipation by setting a characteristic length. An adaptive mesh refinement process is incorporated to allow large shear strains. Remeshing is triggered by a combination of error estimators and mesh distortion indicators. For a more detailed description of the numerical approach of ELFEN, we refer to Crook et al. (2006), who have shown that by an appropriate choice of a constitutive law with generic (i.e. not measured precisely) properties for the model material, a good correspondence with the evolving first-order structures in sandbox experiments is obtained. The method used by Crook et al. (2006) is justified by the fact that the required set of material properties of model materials under the appropriate (i.e. stress) conditions has never been accurately and completely measured up to now, and doing this in the future requires significant development of instrumentation.

The geometry and boundary conditions of the numerical model in this study are chosen to represent typical conditions in corresponding sandbox experiments (e.g., Adam et al., 2005; Schmatz et al., 2010; Horsfield, 1977), with the additional assumption of plane strain (Fig. 1). The sand is 400 mm wide and 140 mm high and overlies a faulted stiff basement with variable normal fault dip. A Coulomb friction interface model is defined to represent the contact between sand and the basement. The top of the model is a free surface.

The finite element mesh is composed of unstructured quadrangles with an initial element size of 4 mm (Fig. 2a). Adaptive remeshing is allowed in two regions to create a finer mesh when a threshold strain is reached. The first region includes the complete overburden and the basement, and the second region contains only the area where localization with large shear strain and high strain gradients is expected to occur (Fig. 2b). In the second region we assigned a minimum element size of approximately 2.0 mm to obtain a shear band width corresponding to that in sandbox experiments (Fig. 2b).

The model runs in two stages: (1) a settling stage and (2) a fault displacement stage. In the settling stage, the equilibrium stress state under a gravitational body force is reached (Fig. 1a). In the displacement stage, the shear process is simulated using the boundary conditions shown in Fig. 1. The maximum displacement on the basement fault is set to 58 mm. (Fig. 3).

A material grid is defined for the overburden part of the model to allow visualization of the deformation independent of remeshing. A set of points, attached to the material grid, is defined to monitor the displacements and velocities in selected points and fault blocks of the model. This significantly increases the calculation time and therefore, only these two properties are monitored in this study.

Material properties (Table 1) are chosen to represent generic sand that is estimated to be typical of existing sandbox experiments. Because at present there is no technique available to completely and accurately measure the properties of materials used in sandbox experiments at the appropriate stress conditions, we do not aim to use precisely and independently measured parameters to accurately match all measurables in our simulations. The parameters used correspond to an “usual” drained sand modeled using an elasto-plastic constitutive law with non-linear elasticity and an initial yield surface (Fig. 4) which is plastic-strain-dependent defined. The basement is modeled as elastic with a Young's modulus of 2.1×10^8 kPa and a density of 7860 kg/m^3. We realize that such a sharp material contrast may be unrealistic in nature and future numerical models could help in understanding its impact on deformation in the overlying sediments.

We varied the basement fault dip between 0° (horizontal block motion) and 90° (trapdoor), in steps of 10° to analyze its impact on the deformation patterns in the overlying sand package. Based on the results of these analyses we subsequently ran a series of additional experiments, varying basement fault dip in 1° increments, between 60° and 70°.

3. Results

3.1. Localization patterns and orientations

A constant basement fault displacement value of 29 mm was selected to compare deformed material grids (Fig. 4). In addition,

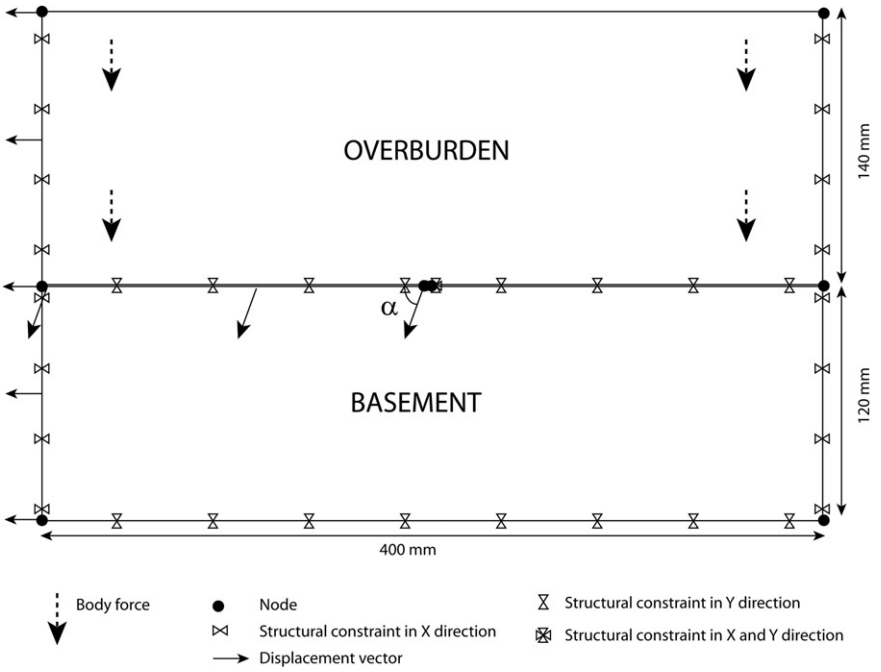

Fig. 1. Set-up of the 2D plane strain finite element model. The model has a width of 400 mm and is composed of two parts: a rigid base and an overburden package of 140 mm thickness. In a first stage, a body force is applied to the overburden to allow the material to settle under its own weight. In a second stage, a displacement is applied on the upper left part of the base, in a direction a, which will determine the final basement fault dip. Structural constraints are applied in *X* and *Y* direction to avoid displacements at the boundaries of the model.

for the resulting structural styles that developed, material grids at three different stages are shown in Fig. 5. In the following, we use the word "shear band" when we refer to structures in the sand and use the word "fault" for describing the basement offset structure.

Regardless of basement fault dip, the shear band in the sand section always starts at the bottom of the sand package at the tip of the basement fault. With continued displacement on the basement fault, the initial shear band migrates upwards to the top of the sand package (Fig. 5). Depending on the dip of the basement fault, different localization patterns develop which are categorized in three domains: (1) *graben domain* for basement fault dip of 60° and less (Fig. 4 a–f), (2) *precursor domain* characterized by a reverse fault transitioning into a normal fault for basement fault dip of 70° and higher (Fig. 4h–j) and (3) a *transitional domain* where a reverse fault is succeeded by normal faulting and then graben formation for basement fault dip between 60° and 70° (Fig. 4g). We first explore the evolution of the two end-member classes in more detail based on the cases in which the orientation of the basement fault dip is 20° and 70° (Fig. 5a–c and g–i). The transitional behavior is illustrated by the example of basement fault dip of 62° in Fig. 5d–f).

When the basement fault dips at 20°, a synthetic normal shear band forms first. With increasing displacement, an antithetic shear band develops and a graben structure is generated (Fig. 5a, b). During the simulation, the plastic strain indicates that there is more deformation on the synthetic shear band than on the antithetic shear band. In a later stage, a secondary antithetic shear band develops forming a secondary graben structure (Fig. 5c). The synthetic normal shear band is wider at the base of the sand package and concave-up. This evolution characterizes the structure defined as a *graben domain*.

When the basement fault dips at 70°, a curved shear band with a dip significantly steeper than the basement fault forms first (Fig. 5g). The dip direction changes along this shear band from synthetic to the basement fault at its base and becomes near-vertical at the top. We refer to this shear band as a precursor. With continued displacement on the basement fault, a second shear band forms with a dip closer to the basement fault dip (Fig. 5h), and all the displacement on the basement fault is accommodated by this shear band (Fig. 5i). The plastic strain is therefore smaller in the precursor shear band than in the main normal fault. This evolution characterizes the structure in the *precursor domain*.

For basement fault dips of 62°, elements of both *structural domains* are present. A precursor forms first, but with increasing displacement, it gradually transitions to a steep synthetic shear band (Fig. 5d–e). Later on, an antithetic shear band forms and a graben structure develops (Fig. 5f). Repetition of the simulation for basement fault dip of 65° results in slightly different results. In a first run, the final shear band pattern is a graben structure whereas in a second run, the antithetic shear band never forms and the graben structure fails to develop. We conclude that there must be some kind of transition region between the two well-defined *structural domains* but the details of this transition region require a more detailed analysis to elucidate and are beyond the scope of this paper.

We also measured the fault dip in the sand sequence as the basement fault dip varied. In the graben domain dips vary from 60 to 67° (basement fault dips 0–50°) while in the precursor domain the dips are higher (73–77° for basement fault dips of 60–80°). Neither Horsfield (1977) nor Egholm et al. (2007) recorded any change in fault dip in the sand sequence for basement fault dips at 30, 45, and 60°, even though Horsfield's experiment with the 60° fault dip lies clearly in the precursor domain. This subject requires more detailed models to clarify whether and under what conditions fault dips do vary as a function of basement fault dip because this outcome may influence theories of fault structure evolution.

As discussed above, structural evolution has a strong effect on the fault zone's internal structure. Although both *structural domains* ultimately produce a master shear band more or less in the same direction as the basement fault, the different early evolution, the

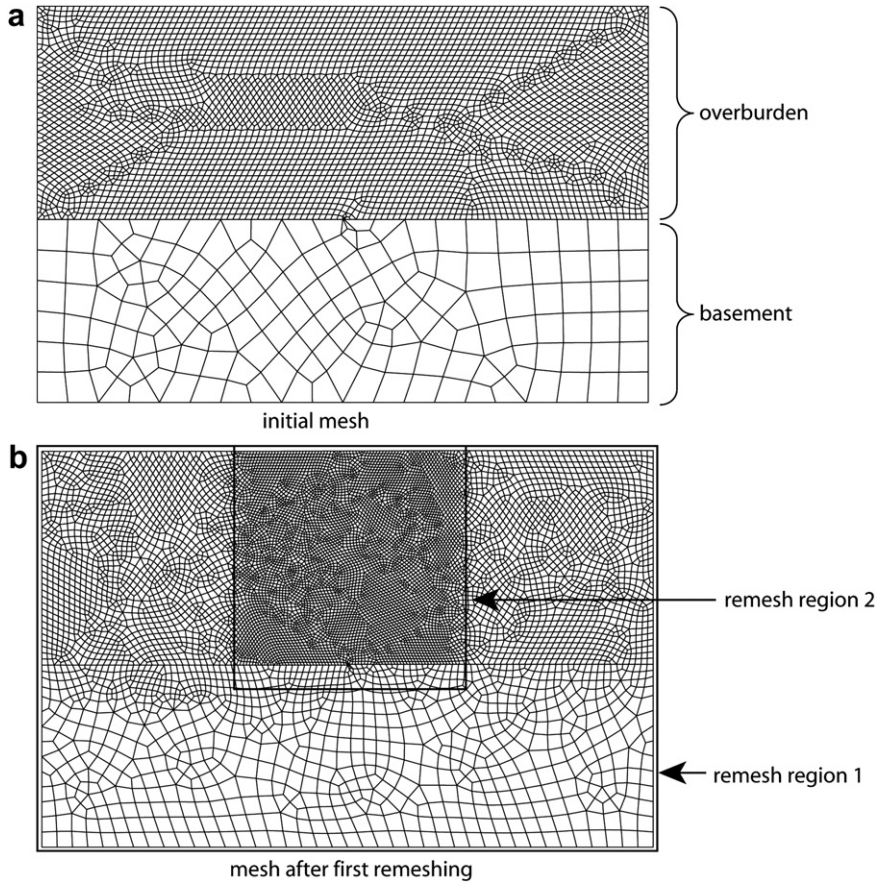

Fig. 2. (a) Initial finite element mesh. The finite element mesh is composed of unstructured quasi-rectangular elements with an initial element size of 4 mm in the sand and 20 mm in the base. (b) Finite element mesh after the first remeshing step. The area with smaller mesh size is the area where localization is expected and where smaller elements are required.

way normal stress on the fault changes (Holland et al., 2011), and the way precursor migrates through the material, can all be expected to lead to differences in fault zone structure.

3.2. Velocity analysis

Different localization patterns develop in the sand with increasing displacement. A hodograph analysis, in which instantaneous velocity vectors of a moving object are translated to the same initial point, provides additional information on how these

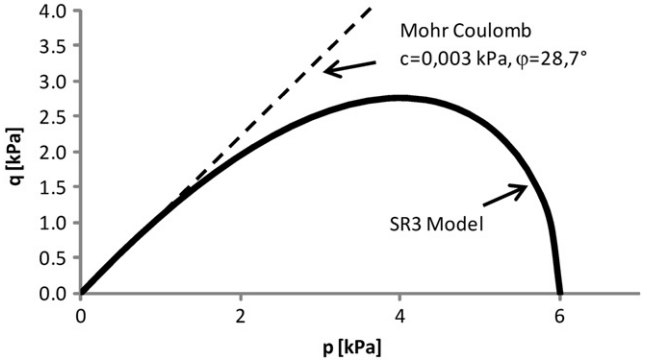

Fig. 3. P-Q diagram (effective mean stress versus differential stress) showing the yield surface.

Table 1
Material parameters of the constitutive law used in our models (see also Crook et al. (2006) for further explanation of the material properties). Yield surface & dilation definition parameters: P_c = Pre-consolidation pressure (end cap), P_t = Tensile intercept, exponent n, a, b_0 and b_1 are material constants which define the shape of the yield surface. Yield surface evolution parameters: P_c (resid) = Residual pre-consoliation pressure, P_t (resid) = Residual tensile pressure, E_{vp} = volumetric elastic strain, λ and κ are hardening constants.

		Crook et al., 2006	This study
Elastic properties	Young's modulus [kPa]	75	500
	Poisson's ratio	0.2	0.4
	Density [kg/m^3]	1560	2000
Yield surface	P_c [kPa]	3	6
	Friction parameter [°]	60	50
	P_t [kPa]	−0.02	−0.01
	Exponent n	Not presented in paper	2
Dilation	Dilatancy angle	50	40
	a	0.25	0.25
	b_0	0.6	0.6
	b_1 [1/kPa]	0.7	0.3
Yield surface evolution	P_c (resid) [kPa]	Not presented in paper	6×10^{-2}
	P_t (resid) [kPa]		-6.89×10^{-3}
	E_{vp} (min)		−0.045
	E_{vp} (max)		0.15
	$\lambda-\kappa$	0.48	0.0385
Regularization parameter	Characteristic length [m]	1.5×10^{-3}	4.5×10^{-3}

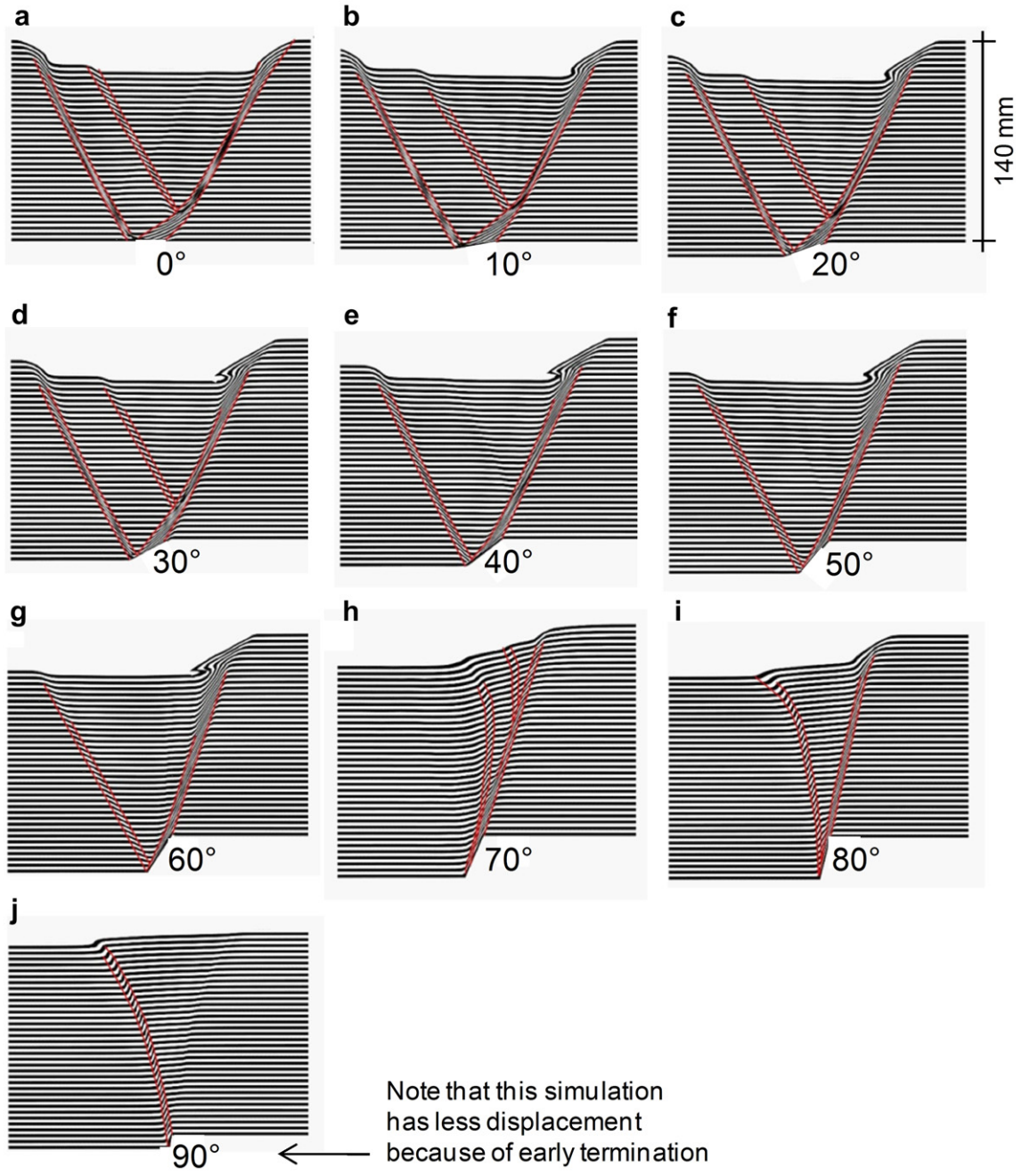

Fig. 4. Deformed material grids shown as passive horizontal marker lines after 29 mm of displacement on the basement fault (except for (j) where the displacement is 9 mm), for different basement fault dips: (a) 0°, (b) 10°, (c) 20°, (d) 30°, (e) 40°, (f) 50°, (g) 60°, (h) 70°, (i) 80°, (j) 90°. The thickness of the sand package is 140 mm in all models. Different shear band patterns are observed. In (a)–(d), a synthetic shear band forms first, followed by an antithetic shear band. Later on, a secondary antithetic shear band is formed, causing a secondary graben structure. In (e)–(g), a graben structure forms without a secondary antithetic shear band. In (h)–(j), a reverse shear band forms first, followed by a normal shear band with dip close to the basement fault dip. The simulation in (j) had numerical instabilities and could therefore only run until a displacement of 9 mm. The folded marker layers in (b)–(g) represent a slope instability.

shear bands change over time. Here, the moving objects are the different fault blocks. The tip of the velocity vector traces a curve defined as the hodograph. In order to differentiate the different blocks that need to be incorporated in the hodograph, we first plot the displacement contours for the *Y* direction for basement fault dips of 20°, 50° and 80° for two different displacements (Fig. 6).

For a basement fault dip of 20° (graben domain) and a very small displacement (2.9 mm), we observe that three major blocks are present: the footwall, the hanging wall (block 1) and a central block (block 2) that has the maximum displacement in the *Y* direction (Fig. 6a). At a displacement of 8.7 mm, the central block is now separated into two blocks (blocks 2 and 3) that move with different velocities. The development of block 3 is the result of the secondary antithetic fault (separating block 2 and block 3). For a basement fault dipping 50° (graben domain), only three blocks are present for both displacements (Fig. 6b) without the development of a secondary antithetic fault. The footwall, the hanging wall (block 1) and the central block 2.

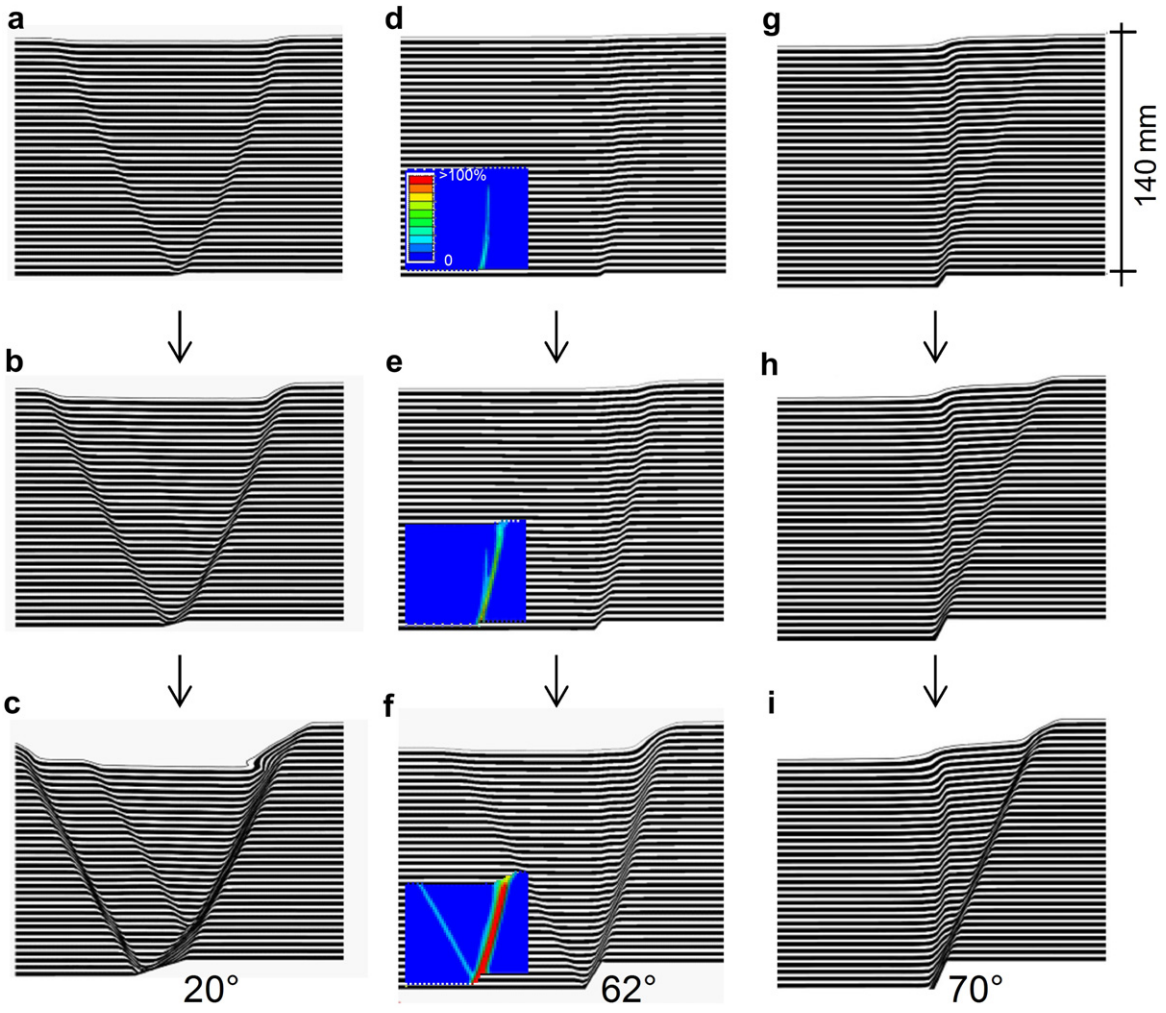

Fig. 5. Deformed material grid shown as passive horizontal marker lines during progressive displacement on a basement fault with dip of (a–c) 20°, (d–f) 62° and (g–h) 70°. Basement fault with dip of 20°: (a) displacement = 4.64 mm, synthetic shear band forms, (b) displacement = 10.44 mm, antithetic shear band has formed, graben structure, (c) displacement = 27.84 mm, secondary antithetic shear band has formed with secondary graben. Basement fault with dip of 62°: (d) displacement = 2.32 mm, a reverse shear band forms, oriented steeper than the basement fault. (e) displacement = 5.8 mm, a synthetic shear band has formed. (f) displacement = 17.4 mm, most displacement is accommodates by the synthetic shear band but additionally, an antithetic shear band develops. For additional explications the evaluated volumetric plastic strains are given in the bottom left of each picture. Basement fault with dip of 70°: (g) displacement = 7.54 mm, a reverse shear band forms, oriented steeper than the basement fault, (h) displacement = 13.34 mm, synthetic shear band has formed (i) displacement = 24.94 mm, all displacement is accommodated by the synthetic shear band.

For a basement fault dip of 80° (precursor domain), we differentiate two bodies, separated by the precursor fault, namely the footwall and block 1, at low displacement (Fig. 6c). At a displacement of 8.7 mm, the precursor fault evolves stepwise toward the main normal fault and hereby develops an arc shape (Fig. 6c). Therefore a 3rd block (central block or block 2) develops. Note that we are unable to differentiate all of these different blocks in the deformed material grid (Fig. 5g).

Based on the velocities of points attached to the material grid in the different blocks, we constructed hodographs for the three cases of basement fault dip at different displacements (Fig. 7). For a basement fault dip of 20°, the dip of the synthetic fault (v_2) is much steeper than the basement fault dip (v_1) (Table 2). To further clarify, vector v_1 represents the displacement of the hanging wall block (block 1) moving at a dip corresponding to the basement fault (given a footwall reference frame). Vector v_2 represents the displacement of block 2, moving at a dip corresponding to the synthetic shear band. Vector v_{12} represents the relative displacement between the block 1 and block 2 (Table 2). As a result of the sharp contrast between the movement of the block 2 and the movement on the basement fault (i.e. vector v_2 and v_1 respectively), a secondary antithetic shear band forms (Fig. 7b). This causes the relative displacement between block 1 and block 2 to be distributed on the two antithetic shear bands, denoted by vectors v_{13} and v_{32} (Fig. 7b) and the "middle block" to be subdivided into two parts. Over time, vector v_3 moves toward vector v_1, corresponding to a decrease in the relative displacement on the primary antithetic shear band and an increase in the relative displacement on the secondary antithetic shear band (Fig. 7c).

For a basement fault dip of 50°, the relative displacements of the blocks in the first stages of displacement are similar to those calculated for a basement fault dip of 20°. However, because the basement fault dip is greater, the contrast between v_1 and v_2 is lower, resulting in a small relative displacement vector v_{12} (Fig. 7d).

For a basement fault dip of 80° (precursor domain), the synthetic shear band dip is shallower than the basement fault dip, in contrast to what was observed in the graben domain. Moreover, an antithetic shear band forms before the synthetic shear band, and this shear band is interpreted as a "precursor" shear band. In Fig. 7g,

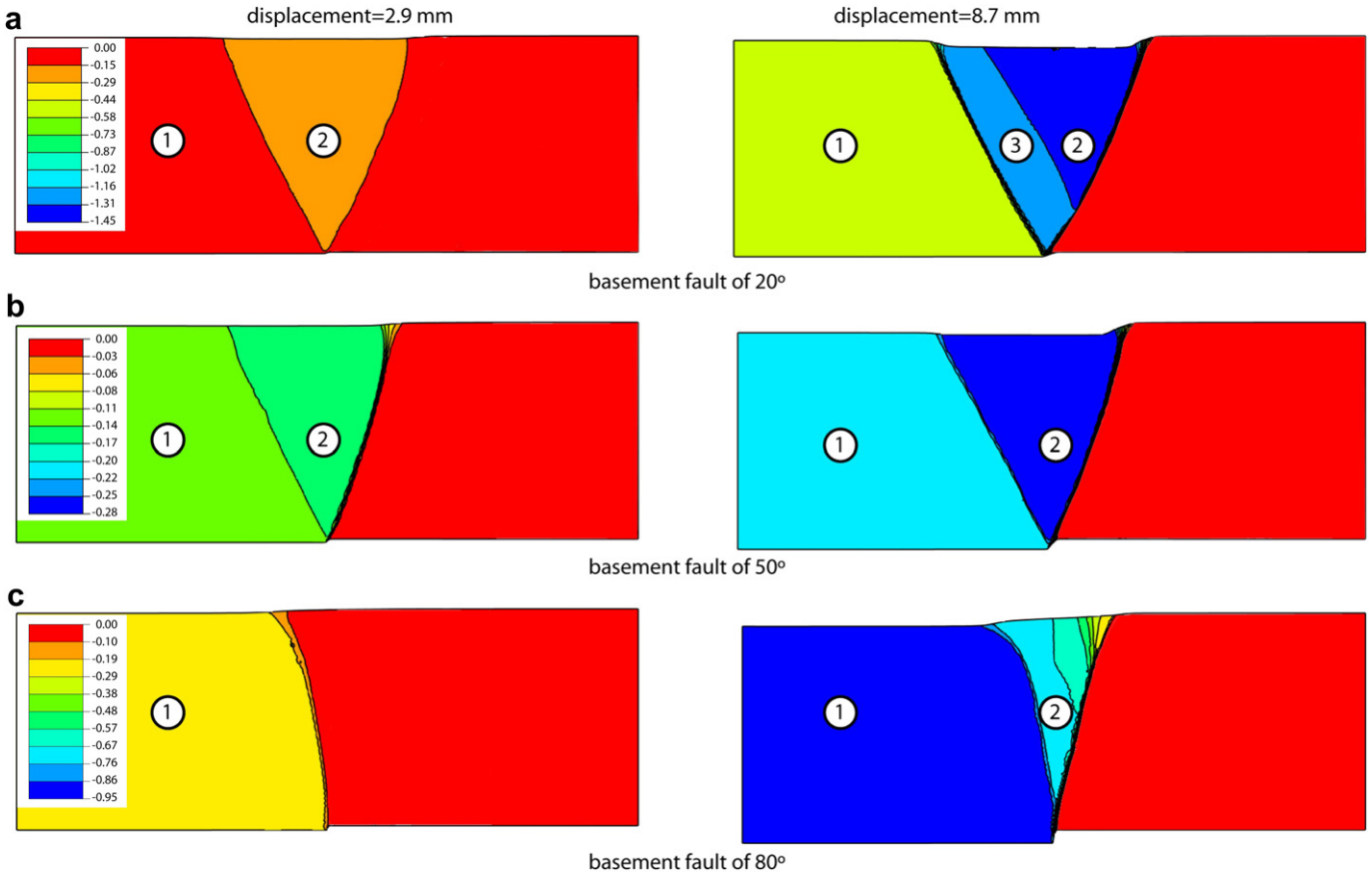

Fig. 6. Contours of (incremental) displacement in *Y* direction (in mm) for basement fault dip of (a) 20°, (b) 50° and (c) 80° at 2.9 mm displacement (left) and 8.7 mm displacement (right). Different blocks are differentiated.

vector v_1 represents the displacement on the hanging wall (block 1) moving at a dip determined by the basement fault, and vector v_2 represents the displacement on the middle block moving at a dip corresponding to the normal shear band. Vector v_{12} then represents the relative displacement on the precursor fault. Over time, displacement on the precursor shear band decreases and the two blocks move as one rigid block (Fig. 7i).

3.3. Stress analysis

The displacement on the basement fault clearly influences the stress state in the overlying sand package. In Fig. 8, maximum and minimum principal stresses are compared for basement fault dips of 20°, 50° and 70°, at the initial stages of deformation and localization.

At the bottom of the sand package, the orientations of the stress axes differ depending on the basement fault dip (Fig. 8). With an increasing steepness of the basement fault dip the inclination of the maximum principle stress is increasing (Fig. 8). As a result, the changing principal stress directions affect the differences in the orientation of the synthetic shear bands. We also observe a counterclockwise rotation of the maximum principal stress, related to the direction of the sense of shear between the hanging wall and footwall.

Similar patterns are described in Patton and Fletcher (1995) where an analytical solution is presented for the elastic stress field above a basement fault. The stress patterns in the finite element model results are more complicated because a small amount of plastic deformation is present. Although a rigorous comparison of analytical and numerical results in elastic models must still be undertaken, the qualitative agreement is sufficient for the goals of the current study.

Additionally, stress rotation around co-seismic faults has also been observed in nature (e.g. Michael, 1987; Hauksson and Jones, 1988; Michael et al., 1990; Hauksson, 1994; King et al., 1994; Hardebeck and Hauksson, 2001; Hardebeck and Michael, 2004; Hickman and Zoback, 2004), and addressed by theoretical studies (Yin and Rogers, 1995) and numerical models (Nüchter and Ellis, 2010), suggesting that this effect may be independent of strain rate. However, additional modeling would be required to confirm this.

4. Discussion

In this study we followed the strategy of Crook et al. (2006) who used reasonably chosen “generic” material properties in ELFEN to model the structural evolution in sandbox experiments and found good agreement in the geometry and evolution of structures between models and experiments. In our models, we see a clear transition between “graben-dominated” and “precursor-dominated” structural styles with a narrow transition where both are present. We interpret this as the two *structural domains* discussed earlier. The geometry and boundary conditions of the finite element model with a basement fault correspond to the experiments described in Horsfield (1977), Adam et al. (2005) and Schmatz et al. (2010).

We now compare the structural style in these sandbox models with the ones observed in numerical models.

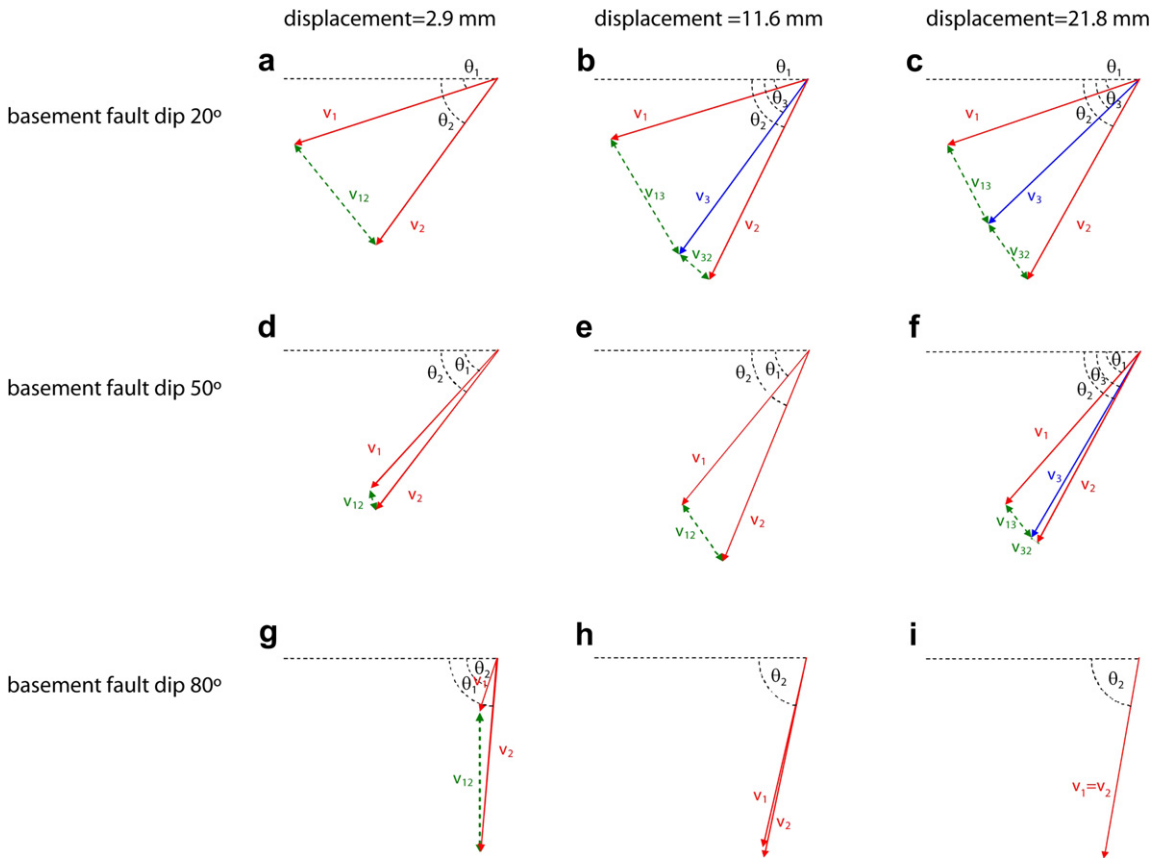

Fig. 7. Displacement vectors and hodograph diagram for basement fault dip of 20°, 50° and 80° at three different displacements (2.9 mm, 11.6 mm and 21.8 mm). For 20°: (a) Stage where normal shear band and antithetic shear band have developed, (b) stage where secondary antithetic shear band has developed and (c) stage where displacement on first antithetic shear band decreases. For 50°: (d) Stage where normal shear band and antithetic shear band have developed, (e) stage where contrast between v_1 and v_2 increases and (f) stage where displacement on secondary antithetic shear band has formed and first antithetic shear band decreases. For 80°: (g) Stage where normal shear band and precursor shear band have developed, (h) stage where contrast between v_1 and v_2 increases and (i) stage where displacement on precursor shear band is equal to the synthetic shear band. v_1 represents the displacement of block 1, v_2 represents the displacement of block 2 and v_3 represents the displacement of block 3, when existing. For fault blocks numbering, we refer to Fig. 6.

4.1. Sandbox models vs. numerical simulations

In the sandbox models of Adam et al. (2005) and Schmatz et al. (2010), a steeply dipping shear band with reverse dip at the top formed at the very early stages of basement fault displacement, followed by initiation of a synthetic shear band at 75° dip. In the finite element model, we observe a similar sequence of shear band formation in the precursor domain, but the dip of the synthetic shear band is 73°. Therefore, there is a clear first-order similarity but also some differences between the numerical and sandbox models.

The results of our study of the effects of basement fault dip are also compared with a series of sandbox experiments, (using different, dry sand) by Horsfield (1977) (Fig. 9). Here, with a basement fault dip of 45° and smaller, a graben structure forms (Horsfield, 1977). With basement fault dips of 60° and higher, a precursor shear band forms, followed by a steep synthetic normal shear band. In these experiments, the synthetic shear band dip is constant (80°) regardless of basement fault dip which is in contrast with the observations in the finite element model where we observe an increase in the synthetic shear band dip with increasing basement fault dip from 60–67° (graben domain) to 73–77° (precursor domain).

Possible explanations for these alternate outcomes are different material properties or differences boundary conditions (e.g. friction at the edges of the experiment, Cubas et al. (2010)).

Table 2
Values incorporated in the hodograph analysis for basement fault dip of 20°, 50° and 80°.

Basement fault dip		Displacement [mm]								
		2.9			11.6			21.8		
		Body 1 (v_1)	Body 2 (v_2)	Body 3 (v_3)	Body 1 (v_1)	Body 2 (v_2)	Body 3 (v_3)	Body 1 (v_1)	Body 2 (v_2)	Body 3 (v_3)
20°	Velocity [mm/s]	6.1	5.9	5.9	5.88	6.43	6.24	5.8	6.6	6
	Dip [°]	20	54.7	54.7	20	64.5	54.8	20	61.1	44.5
50°	Velocity [mm/s]	5.38	5.78		5.76	6.59		5.86	6.25	6.2
	Dip [°]	50	52.7		50	67.7		50	62.1	60.8
80°	Velocity [mm/s]	5.52	1.58		5.82	5.53		5.79	4.79	
	Dip [°]	80	71.57		80	77.47		80	80	

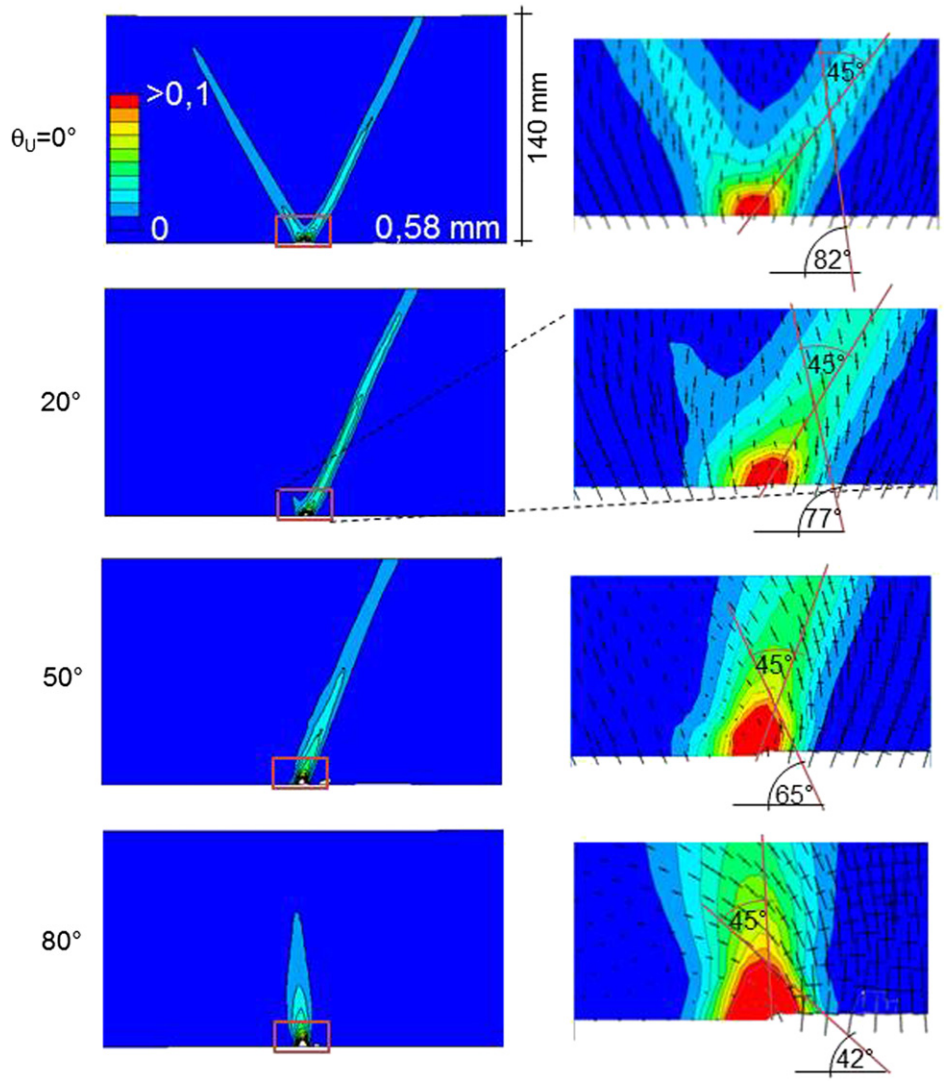

Fig. 8. Plots of the plastic strain contour (left) and maximum and minimum principal stress axes (right) after a displacement of 0.58 mm for 0° basement fault dip, 20° basement fault dip, 50° basement fault dip and 80° basement fault dip. The plastic strain contours show that at this displacement, localization has just started at the bottom of the sand package. The red box on the left shows the location of the enlarged image on the right. The principal stresses at the basement fault show a counterclockwise rotation compared to the basement fault. The angle at the bottom of the pictures on the right indicates the angle between the maximum principal stress and the angle of the shear band-45°. The difference in these angles for the different basement fault dips indicates that the orientation of the maximum principal stress varies with varying basement fault dip. (For interpretation of the references to colour in this figure legend, the reader is referred to the web version of this article.)

Nevertheless, there is a clear first-order similarity and the *structural domains* are reproduced, but there are second-order differences between the numerical and sandbox models. Therefore, we state that the occurrence of a *structural domain* is insensitive to small differences in initial conditions or changes in material properties.

On the other hand, the differences may also be due to aspects of the sand's constitutive behavior that are currently not incorporated in the constitutive law and/or modeling scheme used in ELFEN. This would mean that even if all required input parameters and boundary conditions are known accurately, there would still be significant differences in localization patterns or displacement fields, which can only be reduced by improving the formulations of the constitutive law itself. In ELFEN, differences in shear band thickness are related to the choice of the element size and the regularization parameters. This is an aspect that is implicit to numerical models. Therefore, we recommend against deriving fault throw-fault thickness relationships based on the results presented in this study.

Finch et al. (2004) and Egholm et al. (2007) also studied the relationship between basement fault dip and localization patterns with discrete element models (DEM). In these models, the *structural domain* is also reproduced but there are second-order differences.

4.2. Precursor faulting as a result of dilatancy

The precursor localization is a process that typically occurs on a sandbox scale, in well-compacted sand and low stress levels and can be avoided by increasing the overburden load (e.g. Schmatz et al., 2010). Other examples where this precursor or reverse fault is observed in deformation of sediments overlying a steep basement fault are described in Sanford (1959), Vendeville (1988), Gawthorpe et al. (1997), and Hardy (2011). For a more detailed description of this effect in analog experiments we refer to Mandl (1988). In both the sandbox and numerical models, a precursor shear band forms before the synthetic shear band for steeply dipping basement fault dips. A useful way to understand the

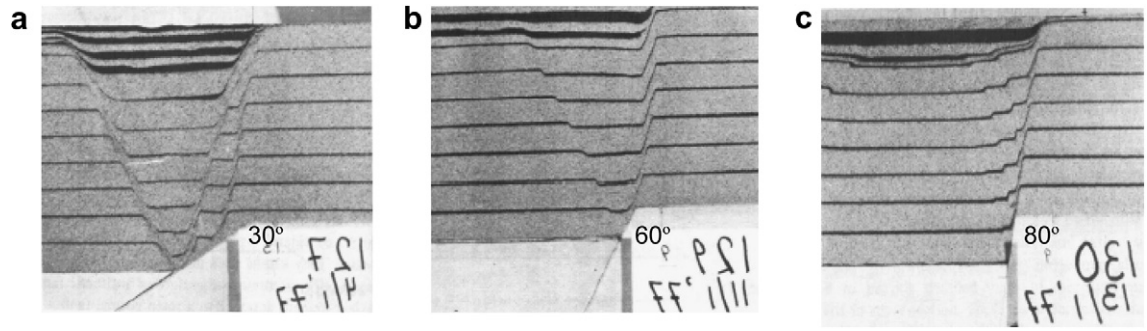

Fig. 9. Final stage of sandbox experiments with sand with varying basement fault dip published in Horsfield (1977). (a) Basement fault dip of 30°, (b) basement fault dip of 60° and (c) basement fault dip of 80°. Total sand layer thickness = 200 mm.

principle of this is to consider that if the model material is able to dilate, the vertical component of displacement results in a volume increase or dilatancy. With steep basement faults, the movement direction resulting from the shear band orientation and the dilatancy angle is not compatible with the basement dip. Therefore, a steeply dipping shear band forms first. During shear band evolution, the dilatancy decreases to zero and the steep shear band is then no longer compatible with the steep basement fault and less steep shear bands develop consecutively.

4.3. Evaluating fault zone structure

One of the objectives of this line of research is to predict the fault zone structure that arises in different *structural domains*. As discussed above, fault evolution has a strong effect on the fault zone's internal structure. Both *structural domains* produce a master shear band more or less in the same direction as the basement fault, but the different early evolution, and the way normal stress on the fault changes (Holland et al., 2011), and the way precursor migrates through the material, can all be expected to lead to fault zone structure changes.

Although the fault structures formed in sand-only systems are simple, the hodographic analysis of fault block displacements holds promise for future studies of more complex systems, by providing an efficient bookkeeping of fault-block evolution (Maillot and Leroy, 2003; Cubas et al., 2008). Moreover, the stress analysis performed helps us decipher when different faults form and in what orientation. Although these results seem insignificant here, this senses as a basis for evaluating more complex systems in future studies.

5. Conclusions

We constructed a "generic" numerical model that produces the essential elements of *structural domains* observed in sandbox experiments. The *structural domain* boundary was explored as a function of basement fault dip. We conclude that these deformation patterns are robust and anticipate they will occur for a range of materials and similar boundary conditions.

We observe two *structural domains* depending on the basement fault dip. For basement fault dips of 60° and lower, a graben structure is formed when an initial synthetic shear band is followed by an antithetic one. For basement fault dips of 70° and higher, a reverse shear band (precursor) is formed, followed by a synthetic, normal shear band. For both end members, the dip of the synthetic shear band shows a correlation with the dip of the basement fault. For basement fault dips between 61° and 70°, the faulting pattern is transitional between the two end members. Simulating the second-order patterns, such as the exact dip and thickness of the shear band, is much more complicated. This is in agreement with the conclusions of the ongoing GeoMod project: the second-order results of modeling geologic processes either in laboratory experiments or with numerical methods depend sensitively on boundary conditions and the numerical method used (Buiter et al., 2006; Schreurs et al., 2006).

Acknowledgments

We acknowledge the technical support from Melanie Armstrong & Tony Crook from Rockfield. We appreciate discussion on the sandbox models with Joyce Schmatz. Thorough reviews by Martin Schoepfer, Nestor Cardozo, Roy Schlische and Jens Nüchter are greatly appreciated and significantly improved the manuscript. This project was funded by ExxonMobil (Unrestricted Research Grant to RWTH-Aachen), and by the German Science Foundation (DFG grants UR 64/10-1 and ZI 714/4-1).

References

Abe, S., van Gent, H., Urai, J.L., 2011. DEM simulation of normal faults in cohesive materials. Tectonophysics 512 (1–4), 12–21.
Abe, S., Urai, J.L., 2012. Discrete element modeling of boudinage: insights on rock rheology, matrix flow, and evolution of geometry. Journal of Geophysical Research B: Solid Earth 117 (1).
Adam, J., Urai, J.L., Wieneke, B., Oncken, O., Pfeiffer, K., Kukowski, N., Lohrmann, J., Hoth, S., van der Zee, W., Schmatz, J., 2005. Shear localisation and strain distribution during tectonic faulting-new insights from granular-flow experiments and high-resolution optical image correlation tehcniques. Journal of Structural Geology 27, 283–301.
Bailey, W.R., Walsh, J.J., Manzocchi, T., 2005. Fault populations, strain distribution and basement fault reactivation in the East Pennines Coalfield, UK. Journal of Structural Geology 27, 913–928.
Buiter, S.J.H., Babeyko, A.Y., Ellis, S., Gerya, T.V., Kaus, B.J.P., Kellner, A., Schreurs, G., Yamada, Y., 2006. The numerical sandbox:comparison of model results for a shortening and an extension experiment. In: Buiter, S.J.H., Schreurs, G. (Eds.), Analogue and Numerical Modelling of Crustal-scale Processes. Geological Society of London Special Publications, London, vol. 253, pp. 29–64.
Crook, A.J.L., Willson, S.M., Yu, J.G., Owen, D.R.J., 2006. Predictive modelling of structure evolution in sandbox experiments. Journal of Structural Geology 28 (5), 729–744.
Cubas, N., Leroy, Y.M., Baillot, B., 2008. Prediction of thrusting sequences in accretionary wedges. Journal of Geophysical Research 113.
Cubas, N., Maillot, B., Barnes, C., 2010. Statistical analysis of an experimental compressional sand wedge. Journal of Structural Geology 32, 818–831.
Egholm, D.L., Sandiform, M., Clausen, O.R., Nielsen, S.B., 2007. A new strategy for discrete element numerical models: 2. Sandbox applications. Journal of Geophysical Research 112.
Ellis, S., Schreurs, G., Panien, M., 2004. Comparisons between analogue and numerical models of thrust wedge development. Journal of Structural Geology 26, 1659–1675.
Finch, E., Hardy, S., Gwathorpe, R., 2004. Discrete-element modelling of extensional fault-propagation folding above rigid basement fault blocks. Basin Research 16, 489–506.
Gawthorpe, R.L., Sharp, I., Underhill, J.R., Gupta, S., 1997. Linked sequence stratigraphic and structural evolution of propagating normal faults. Geology 25, 795–798.
Gudehus, G., Karcher, C., 2006. Hypoplastic simulation of normal faults without and with clay smears. Journal of Structural Geology 29 (3).

Hardebeck, J.L., Hauksson, E., 2001. Crustal stress field in southern California and its implications for fault mechanics. Journal of Geophysical Research 106, 21,859–21,882.
Hardebeck, J., Michael, A., 2004. Stress orientations at intermediate angles to the San Andreas fault, California. Journal of Geophysical Research 109 (B11303). doi:10.1029/2004JB003239.
Hardy, S., 2011. Cover deformation above steep, basement normal faults: insights from 2D discrete element modeling. Marine and Petroleum Geology 28, 966–972.
Hauksson, E., 1994. State of stress from focal mechanisms before and after the 1992 Landers earthquake sequence. Bulletin of the Seismology Society of America 84, 917–934.
Hauksson, E., Jones, L.M., 1988. The July 1986 Oceanside (ML = 5.3) earthquake sequence in the continental borderland, southern California. Bulletin of the Seismology Society of America 78, 1885–1906.
Hickman, S., Zoback, M., 2004. Stress orientations and magnitudes in the SAFOD pilot hole. Geophysical Research Letters 31 (L15S12). doi:10.1029/2004GL020043.
Higgins, R.I., Harris, L.B., 1997. The effect of cover composition on extensional faulting above re-activated basement faults: results from analogue modelling. Journal of Structural Geology 19, 89–98.
Holland, M., Urai, J.L., Martel, S., 2006. The internal structure of fault zones in basaltic sequences. Earth and Planetary Science Letters 248 (1–2), 286–300.
Holland, M., van Gent, H., Bazalgette, L., Yassir, N., Hoogerduijn-Strating, E., Urai, J.L., 2011. Evolution of dilatant fracture networks in normal faults - evidence from 4D model experiments. Earth and Planetary Science Letters 304, 399–406.
Horsfield, W.T., 1977. An experimental approach to basement-controlled faulting. Geologie en Mijnbouw 56 (4), 363–370.
Kenis, I., Urai, J.L., van der Zee, W., Hilgers, C., Sintubin, M., 2005. Rheology of fine-grained siliciclastic rocks in the middle crust – Evidence from structural and numerical analysis. Earth and Planetary Science Letters 233 (3–4), 351–360.
King, G.C.P., Stein, R.S., Lin, J., 1994. Static stress changes and the triggering of earthquakes. Bulletin of the Seismology Society of America 84, 935–953.
Maillot, B., Leroy, Y.M., 2003. Optimal dip based on dissipation of back thrusts and hinges in fold-and-thrust belts. Journal of Geophysical Research 108.
Mandl, G., 1988. Mechanics of Tectonic Faulting: Models and Basic Concepts. Elsevier, Amsterdam.
Mandl, G., 2000. Faulting in Brittle Rocks. Springer.
Michael, A.J., 1987. Stress rotation during the Coalinga aftershock sequence. Journal of Geophysical Research 92, 7963–7979.
Michael, A.J., Ellsworth, W.L., Oppenheimer, D.H., 1990. Coseismic stress changes induced by the 1989 Loma Prieta, California earthquake. Geophysical Research Letters 17, 1441–1444.
Nüchter, J., Ellis, S., 2010. Complex states of stress during the normal faulting seismic cycle: role of midcrustal postseismic creep. Journal of Geophysical Research 115. doi:10.1029/2010JB007557.
Panien, M., Buiter, S.J.H., Schreurs, G., Pfiffner, A., 2006. Inversion of a symmetric basin: insights from a comparison between analogue and numerical experiments. In: Buiter, S.J.H., Schreurs, G. (Eds.), 2006. Geological Society of London, Special Publications, London, vol. 253, pp. 253–270.
Patton, T.L., 2005. Sandbox models of downward steepening normal faults. AAPG Bulletin 89 (6), 781–797.
Patton, T.L., Fletcher, R.C., 1995. Mathematical block-motion for deformation of a layer above a buried fault of arbitrary dip and sense of slip. Journal of Structural Geology 17 (10), 1455–1472.
Richard, P., 1991. Experiments on faulting in a two-layer cover sequence overlying a reactivated basement fault with oblique-slip. Journal of Structural Geology 13, 459–469.
Sanford, A.R., 1959. Analytical and experimental study of simple geologic structures. Bulletin of the Seismology Society of America 70, 19–52.
Schmatz, J., Vrolijk, P.J., Urai, J.L., 2010. Clay smear in normal fault zones – the effect of multilayers and clay cementation in water-saturated model experiments. Journal of Structural Geology 32 (11), 1834–1849.
Schöpfer, M.P.J., Childs, C., Walsh, J.J., Manzocchi, T., Koyi, H.A., 2007a. Geometrical analysis of the refraction and segmentation of normal faults in periodically layered sequences. Journal of Structural Geology 29, 318–335.
Schöpfer, M.P.J., Childs, C., Walsh, J.J., 2007b. 2D Distinct Element modeling of the structure and growth of normal faults in multilayer sequences. Part 2: impact of confining pressure and strength contrast on fault zone geometry and growth. Journal of Geophysical Research 112.
Schöpfer, M.P.J., Childs, C., Walsh, J.J., 2009a. The impact of porosity and crack density on the elasticity, strength and friction of cohesive granular materials: insights from DEM modelling. International Journal of Rock Mechanics & Mining Sciences 46 (2), 250–261.
Schöpfer, M.P.J., Childs, C., Walsh, J.J., 2009b. Two-dimensional Distinct Element Method (DEM) modeling of tectonic fault growth in mechanically layered sequences. In: Kolymbas, D., Viggiani, G. (Eds.), Mechanics of Natural Solids. Springer, Heidelberg, pp. 127–146.
Schreurs, G., Buiter, S.J.H., Boutelier, D., Corti, G., Costa, E., Cruden, A.R., Daniel, J.-M., Hoth, S., HKoyi, H.A., Kukowski, N., Lohrmann, J., Ravaglia, A., Schlische, R.W., Withjack, M.O., Yamda, Y., Cavozzit, C., Delventisette, C., Elder Brady, J.A., Hoffmann-Rothe, A., Mengus, J.-M., Montanari, D., Nilforoushan, F., 2006. Analogue becnhmarks of shortening and extension experiments. In: Buiter, S.J.H., Schreurs, G. (Eds.), Analogue and Numerical Modelling of Crustal-scale Processes. Geological Society of London Special Publications, London, vol. 253, pp. 1–27.
Schultz-Ela, D.D., Walsh, P., 2002. Modeling of grabens extending above evaporites in Canyonlands National Park, Utah. Journal of Structural Geology 24, 247–275.
Taniyama, H., 2011. Numerical analysis of overburden soil subjected to strike-slip fault: distinct element analysis of Nojima fault. Engineering Geology 123, 194–203.
Tsuneishi, Y., 1978. Geological and experimental studies on mechanism of block faulting. Bulletin of the Earthquake Research Institute (Japan) 53, 173–242.
van der Zee, W., Urai, J.L., 2005. Processes of normal fault evolution in a siliciclastic sequence: a case study from Miri, Sarawak, Malaysia. Journal of Structural Geology 27, 2281–2300.
van der Zee, W., Urai, J.L., Richard, P., 2003. Lateral clay injection into normal faults. GeoArabia 8 (3), 501–521.
van der Zee, W., Wibberley, C.A.J., Urai, J.L., 2008. The influence of layering and pre-existing joints on the development of internal structure in normal fault zones. The Lodève Basin, France. Geological Society Special Publication 299, 57–74.
van Gent, H., Holland, M., Urai, J.L., Loosveld, R., 2010a. Evolution of fault zones in carbonates with mechanical stratigraphy – Insights from scale models using layered cohesive powder. Journal of Structural Geology 32 (9), 1375–1391.
van Gent, H., Back, S., Urai, J.L., Kukla, P., 2010b. Small-scale faulting in the Upper Cretaceous of the Groningen block (the Netherlands): 3D seismic interpretation, fault plane analysis and regional paleostress. Journal of Structural Geology 32 (4), 537–553.
Vendeville, B.C., 1988. Scale-models of basement induced-extension. Comptes Rendus de ÍAcadémie des Sciences 307, 1013–1019.
Welch, M.J., Knipe, R.J., Souque, C., Davies, R.K., 2009. A Quadshear kinematic model for folding and clay smear development in fault zones. Tectonophysics 471, 186–202.
Withjack, M.O., Olson, J.E., Peterson, E., 1990. Experimental models of extensional forced folds. AAPG Bulletin 74 (7), 1038–1054.
Yin, Z., Rogers, G., 1995. Rotation of the principal stress directions due to earthquake faulting and its seismological implications. Bulletin of the Seismology Society of America 85, 1513–1517.